J. Fluid Mech. (2005), *vol.* 540, *pp.* 221–245. © 2005 Cambridge University Press
doi:10.1017/S002211200500580X Printed in the United Kingdom

External turbulence interaction with a columnar vortex

By J. S. MARSHALL AND M. L. BENINATI

Department of Mechanical and Industrial Engineering, and IIHR – Hydroscience and Engineering, The University of Iowa, Iowa City, IA 52242, USA

(Received 11 February 2004 and in revised form 25 April 2005)

A study was performed using direct numerical simulation to examine the interaction of external turbulence with a nominally columnar, large-scale vortex at a vortex Reynolds number $Re_V \equiv \Gamma/\nu = 3000$. A multi-step procedure is used to generate initial conditions in which the external turbulence has the wrapped, nearly azimuthal form characteristic of turbulence around a large-scale vortex structure. The proper-orthogonal decomposition method is used to extract specific modes of the vortex turbulence that dominate the kinetic energy and enstrophy fields. The effect of turbulence initial intensity and length scale on the turbulence structure and its influence on the large-scale vortex are examined. It is observed that the external turbulence wraps around the large-scale vortex and advects radially inward toward the vortex core. The dominant axial length scale of the external turbulence appears to scale with the vortex core diameter, with the mode with the largest enstrophy having a wavelength of about twice the core diameter. The turbulence induces a bending wave on the vortex core with axial wavelength approximately equal to the dominant wavelength of the external turbulence. The turbulent enstrophy decays according to a power-law expression for cases with moderate initial turbulence intensity. For sufficiently strong initial turbulence intensity, the turbulence breaks up the large-scale vortex core, creating strong turbulence within the vortex core.

1. Introduction

Most high-Reynolds-number flows are dominated, at some scale, by tube-like vortex structures. In some applications these vortex structures dominate the mean flow field, as is the case for airfoil tip vortices, ship and airplane hull vortices, juncture vortices about pilings of control surfaces, pump-intake vortices, and helicopter rotor and propeller wake vortices. In a large number of other flows, these vortex structures might not be readily observable in the mean flow field but may nevertheless dominate turbulence at a slightly smaller scale. For instance, tube-like coherent vortices control turbulent species mixing rates, heat transfer, turbulence production rates, and momentum transport in turbulent wall layers, mixing layers, jets, and bluff-body wakes. While there are several instabilities that may lead to breakup of large-scale vortices (e.g. Crow 1970; Lessen, Singh & Paillet 1974), interaction of vortices with small-scale external turbulence is known to dominate vortex breakup and decay in certain situations where the external turbulence is sufficiently strong (Tombach 1973; Liu 1992). Understanding the interactions of large-scale vortex structures with surrounding smaller-scale turbulence is crucial for modelling turbulence physics, in addition to development of new methods for control of high-Reynolds-number fluid flows occurring in many engineering applications.

https://doi.org/10.1017/S002211200500580X Published online by Cambridge University Press

There have been several computational and experimental studies of vortex–turbulence interaction, a review of which is given by Marshall & Beninati (2000). A flow visualization study by Sarpkaya & Daly (1987) observed intermittent vortex 'bursting' when a vortex is exposed to grid-generated turbulence in a water flume. A wind-tunnel study by Bandyopadhyay, Stead & Ash (1991) examined interaction of a large-scale columnar vortex generated by a pair of oppositely pitched airfoils with turbulence generated by an upstream screen or grid. They observed that the core fluid of the columnar vortex is intermittently ejected outward, and that this exchange of fluid and momentum is controlled by organized vortical motions that wrap around the vortex just outside the core. Bandyopadhyay *et al.* (1991) also observe that there exist intermittent patches of highly turbulent and relaminarized fluid in the columnar vortex core. The relaminarization is hastened by suppression of turbulence by the solid-body rotation within the vortex core (Bradshaw 1969), and the intermittent high-turbulence patches are probably a result of interaction of the vortex with external turbulence.

A recent wind-tunnel study of vortex interaction with external turbulence by Beninati & Marshall (2005) used a four-sensor miniature hot-wire probe to examine the various spectral components of the turbulence and vortex response. The vortex is generated in this study using a four-blade vortex generator with a central hub, which is specifically designed to minimize introduction of upstream perturbations leading to vortex wandering. The study observes significant turbulent kinetic energy within the central part of the vortex core, even far downstream of the generation point. This turbulence within the central core appears to be dominated by a bending wave with wavelength ranging from 1 to 3 times the core diameter, in agreement with the flow visualization results of Bandyopadhyay *et al.* (1991). Measurements at different downstream locations indicate that these bending waves are induced by the turbulence, rather than propagated from an upstream location.

Melander & Hussain (1993*a*, *b*) used direct numerical simulation (DNS) to examine interaction between a columnar vortex and initially homogeneous small-scale turbulence. For cases where the turbulence strength is sufficiently low, they observed that the external turbulence structures wrap around the columnar vortex, forming nearly azimuthally oriented rings with azimuthal vorticity of approximately alternating sign as one progresses axially along the core. When the initial turbulence strength is somewhat higher, Melander & Hussain observed that bending waves form on the large-scale vortex. For still stronger magnitude of the initial homogeneous turbulence, the vortex quickly breaks up in the computations. However, the vortex breakup in these computations is not representative of actual coherent vortex interaction with strong external turbulence due to the fact that the vortex breakup occurs while the turbulence is still in a small-scale, nearly homogeneous condition, rather than in the nearly axisymmetric wrapped condition characteristic of turbulence surrounding a columnar vortex.

The process of vorticity ejection (or 'stripping') induced by external wrapped vortex structures was examined by Marshall (1997) using a simplified axisymmetric model consisting of periodically positioned vortex rings around a columnar vortex. It was observed that weak vortex rings induce standing waves of variable core area on the columnar vortex, whereas stronger vortex rings cause vorticity to be stripped and advected radially outward from the columnar vortex in thin sheets that wrap around the vortex rings. Miyazaki & Hunt (2000) used rapid-distortion theory (RDT) to examine the process by which initially homogeneous turbulence becomes axisymmetric and the interaction of this axisymmetric turbulence with a columnar vortex. The RDT results were used to obtain insight into induction of a variety of different wave motions on the columnar vortex by the external turbulence, including axisymmetric and

https://doi.org/10.1017/S002211200500580X Published online by Cambridge University Press

bending waves, although the restriction to linear theory prohibited the computations from examining the large-scale distortions and vorticity stripping processes that lead to breakup of the large-scale vortex. Risso, Corjon & Stoessel (1997) reported a DNS study of vortex pair decay in the presence of external turbulence which indicates that the small-scale turbulence excites perturbations of the vortex pair that enhance development of the mutual-induction instability.

The present paper reports a computational study of the effect of external turbulence on an initially columnar vortex. Rather than starting with homogeneous turbulence, we employ a multi-step initialization procedure leading to an initial state in which the turbulence is wrapped around the large-scale vortex core, in the nearly azimuthal form characteristic of turbulence in the vicinity of a large-scale columnar vortex. This initial condition is achieved using a preliminary computation in which weak turbulence wraps around a columnar vortex, followed by a procedure in which the columnar vortex and a region surrounding the vortex is extracted, the external turbulence strength is modified, and a new columnar vortex is introduced. The interaction of the external turbulence with the initially columnar vortex is examined for different turbulence strengths and length scales.

The numerical method used in the study is described in § 2, along with the procedure for development of the turbulence initial condition. The structure of a vortex with external turbulence is examined in detail in § 3 for a case with external turbulence of moderate strength. We examine the structure of coherent vortices around the turbulent vortex, physical processes occurring during vortex interaction with the external turbulence, various turbulence averages generated by the turbulent vortex structure, and the spectral variation of the energy and enstrophy fields of the vortex turbulence. In § 4, we examine various mechanisms for enhancement and decay of the vorticity field within the external turbulence. Analysis of the flow using proper orthogonal decomposition (POD) is discussed in § 5, where it is used to extract dominant wavenumber modes of the vortex turbulence. The effect of initial external turbulence intensity and length scale on its interaction with the columnar vortex is examined in § 6. Conclusions are given in § 7.

2. Numerical method

The computations are performed using a Fourier pseudo-spectral method similar to that described by Vincent & Meneguzzi (1991), which employs second-order Adams–Bashforth time stepping for nonlinear terms and exact integration of the viscous term. The computations are dealiased using the standard two-thirds wavenumber truncation. The spectral Navier–Stokes equation is evolved in time after having been projected onto a divergence-free space using the operator $P_{ij} = k_i k_j / k^2 - \delta_{ij}$, giving (Vincent & Meneguzzi 1991)

$$\hat{\boldsymbol{u}}^{n+1} = \hat{\boldsymbol{u}}^n \exp(-\nu k^2 \Delta t) + \Delta t\, \boldsymbol{P} \cdot \left[\tfrac{3}{2}\widehat{(\boldsymbol{u} \times \boldsymbol{\omega})}^n \exp(-\nu k^2 \Delta t) - \tfrac{1}{2}\widehat{(\boldsymbol{u} \times \boldsymbol{\omega})}^{n-1} \exp(-2\nu k^2 \Delta t)\right] \tag{1}$$

where $\boldsymbol{u}$ and $\boldsymbol{\omega}$ are the velocity and vorticity vectors, a hat denotes Fourier transform, a superscript indicates the time step, ν is the kinematic viscosity, Δt is the time increment, and δ_{ij} is the Kronecker delta. The velocity and vorticity transforms are related by

$$\hat{\boldsymbol{\omega}} = \mathrm{i}\boldsymbol{k} \times \hat{\boldsymbol{u}}. \tag{2}$$

One of the principal features of the current study is that the computations are initialized by exposing an initially columnar vortex to turbulence that has the wrapped,

https://doi.org/10.1017/S002211200500580X Published online by Cambridge University Press

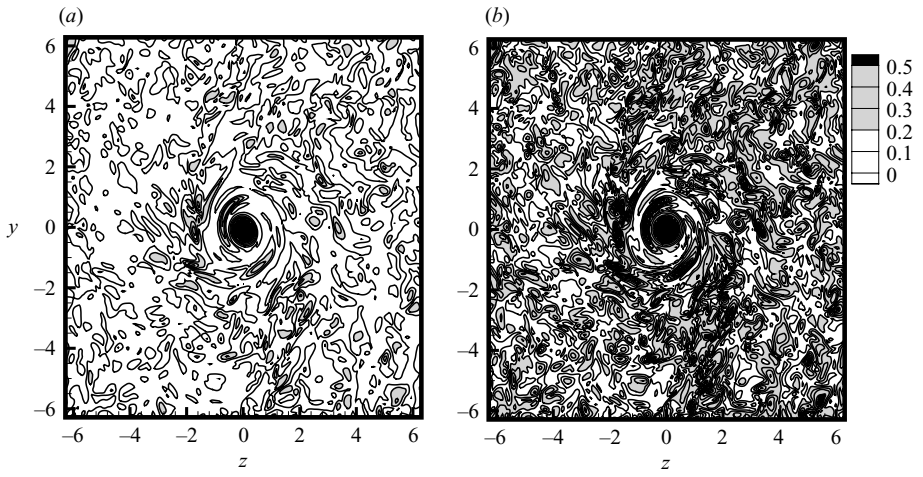


FIGURE 1. Slices of the flow field in the (y, z)-plane showing contours of vorticity magnitude at different stages of the flow initialization process: (a) flow at the end of the 'initialization run' and (b) initial condition for the 'final run' obtained by cutting out the vortex in (a), magnifying the turbulence vorticity with $f_{magn} = 2$, making the vorticity field divergence-free, and adding an unperturbed columnar vortex.

nearly axisymmetric structure characteristic of turbulence near a large-scale vortex, rather than homogeneous turbulence. This effect is achieved using the following initialization sequence:

Step 1: Introduce random velocity fluctuations, having root-mean-square velocity fluctuation u_{rms} and uniform probability distribution for wavenumbers in the range $k_1 < k < k_2$.

Step 2: Set vorticity equal to zero within a cylinder of radius $a_{0,\max}$ along the x-axis.

Step 3: Introduce a columnar vortex of radius $a_0 < a_{0,\max}$ and strength Γ with axis coincident with the x-axis (figure 1a).

Step 4: Perform an 'initialization run' out to a time t_0 in order to let the turbulence develop a form characteristic of that near a columnar vortex.

Step 5: Set vorticity equal to zero within a cylinder of radius $a_{\max}$ along the x-axis.

Step 6: Increase the vorticity magnitude in the remaining external turbulence by a factor f_{magn}.

Step 7: Introduce a vorticity field within the cut-off cylinder of the form

$$\omega_x = (\Gamma/\pi a^2)\exp(-r^2/a^2), \tag{3}$$

corresponding to a columnar vortex oriented in the x-direction with core radius $a < a_{\max}$ and strength Γ (figure 1b).

Step 8: Compute the initial velocity field for the 'final run' by solving for $\hat{\boldsymbol{u}}$ from (2) and then taking the inverse fast Fourier transform.

After each step of this process, and at the end of each time step during the computation, the velocity field is made divergence-free by taking its Fourier transform and using the spectral form of the continuity equation, $\boldsymbol{k} \cdot \hat{\boldsymbol{u}} = 0$, and then the vorticity is recomputed using (2) and the inverse transform is taken to obtain the corrected vorticity and velocity fields in physical space.

Computational variables are non-dimensionalized using the vortex core diameter d and the nominal vortex circulation $\Gamma_n = (\pi/4)\, d^2 \omega_{0,\max}$ to obtain a characteristic length scale (d) and time scale (d^2/Γ_n) for the flow. The vortex Reynolds number is fixed at

https://doi.org/10.1017/S002211200500580X Published online by Cambridge University Press

Case	k_1	k_2	f_{magn}
A	10	30	1
B	5	10	1
C	10	30	0.5
D	10	30	2
E	10	30	3
F	10	30	4

TABLE 1. Summary of computational cases examined, showing truncation wavenumbers of the initial homogeneous turbulence used in the initialization procedure (k_1 and k_2) and the magnification factor of the external turbulence (f_{magn}).

$Re_V = \Gamma_n/\nu = 3000$ for all computations. This value is about an order of magnitude greater than the Reynolds number of coherent eddies in a turbulent boundary layer for a typical laboratory-scale engineering experiment (Marshall 2003), and about four orders of magnitude smaller than the Reynolds number of a typical airplane trailing vortex. The average Kolmogorov length scale at the initial time of the computations (following Step 8 above) is about equal to the grid increment $\Delta x = 0.05$. Because the axial vorticity of the vortex is chopped off at a radius $a_{\max} = 0.65$, the actual vortex circulation is slightly less than unity ($\Gamma = 0.815$) . The value of u_{rms} chosen in Step 1 is sufficiently small that the external turbulence has a small effect on the columnar vortex during the computation in Step 4 of the process. The principal differences in the various computations are the turbulence magnification factor f_{magn} and the initial wavenumber range (k_1, k_2) for the homogeneous turbulence. The time step for all computations is $\Delta t = 0.01$, resulting in a CFL number, $u_{\max}\Delta t/\Delta x$, of less than 0.1 for all cases considered. The computation described in Step 4 of the initialization sequence is carried out to a time $t_0 = 40$, which is sufficient to let the external turbulence attain an approximately axisymmetric structure typical of turbulence around a columnar vortex without being so long as to allow significant degradation of the columnar vortex by the surrounding turbulence. The computational results are not found to be sensitive to the choice of t_0. A listing of the parameter values for all runs performed is given in table 1. The profiles of the turbulent kinetic energy, $\overline{u'^2} \equiv \overline{u_x'^2} + \overline{u_r'^2} + \overline{u_\theta'^2}$, at the initial time of the final run (following Step 8) for all cases considered are plotted in figure 2.

All computations are performed on a rectangular $128 \times 256 \times 256$ domain with side length 2π in the x-direction and 4π in the y- and z-directions. The boundary conditions are periodic on all sides. Tests were conducted with double the domain length in the x-direction, but the flow features, and their variation with axial wavenumber, were essentially unchanged. It was not possible with our machine memory limitations to conduct tests with twice the flow domain in the lateral (y and z) direction while maintaining the same resolution. However, we note that the most energetic region of the external turbulence is located between about $1 < r < 3$, such that the distance between the most energetic turbulence structures and the centre of the large-scale vortex measures between 10 % and 25 % of the lateral domain width.

3. Structure of a vortex with external turbulence

Turbulence structures external to a large-scale columnar vortex wrap around the vortex, forming secondary vortex loops with approximately azimuthal orientation.

https://doi.org/10.1017/S002211200500580X Published online by Cambridge University Press

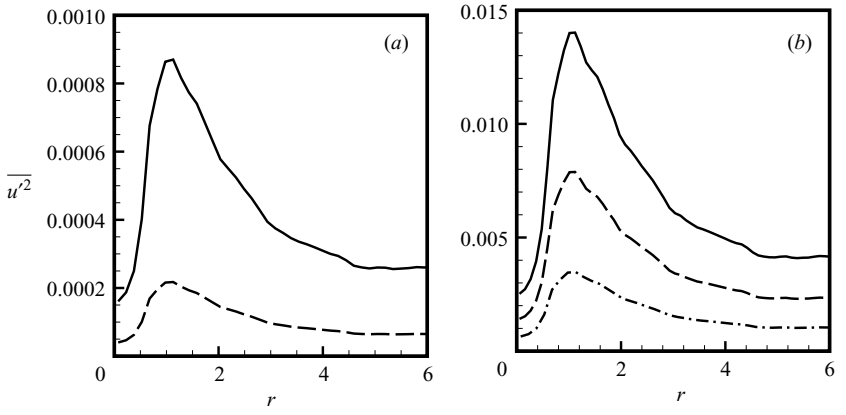


FIGURE 2. Profile of the initial turbulent kinetic energy, $\overline{u'^2} \equiv \overline{u_x'^2} + \overline{u_r'^2} + \overline{u_\theta'^2}$, for cases with (*a*) $f_{magn} = 0.5$ (dashed line) and 1 (solid line) (Cases C and A) and (*b*) $f_{magn} = 2$ (dashed-dotted line), 3 (dashed line) and 4 (solid line) (Cases D, E and F).

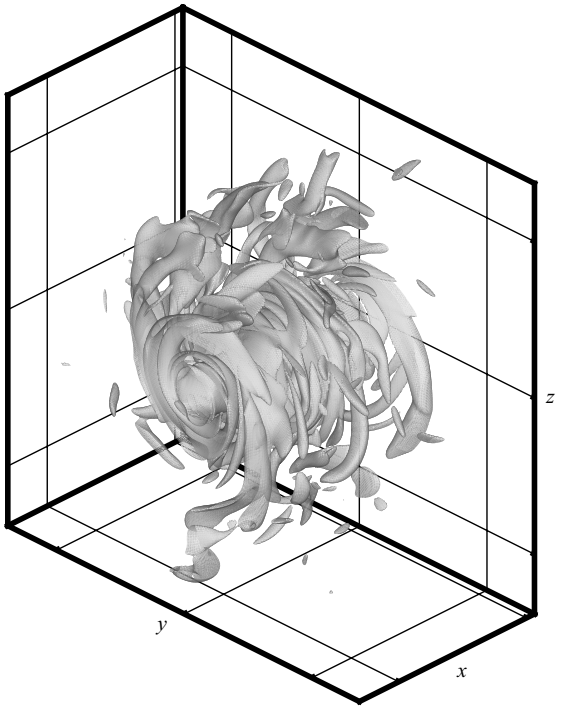


FIGURE 3. Iso-surface of vorticity magnitude $\omega = 0.1$ for Case A at time $t = 100$, showing the external turbulence structures wrapping around the vortex core.

Concurrent with development of these wrapped vortex structures is a temporal increase in the core size of the external turbulence. The wrapping of the external turbulent structures around the columnar vortex is examined in the current section for Case A in table 1 (with $f_{magn} = 1$), unless otherwise indicated. In figure 3, we plot an iso-surface with vorticity magnitude $\omega = 0.1$ illustrating this wrapping process. The external turbulence loop structures each consist of two 'legs' of opposite sign

https://doi.org/10.1017/S002211200500580X Published online by Cambridge University Press

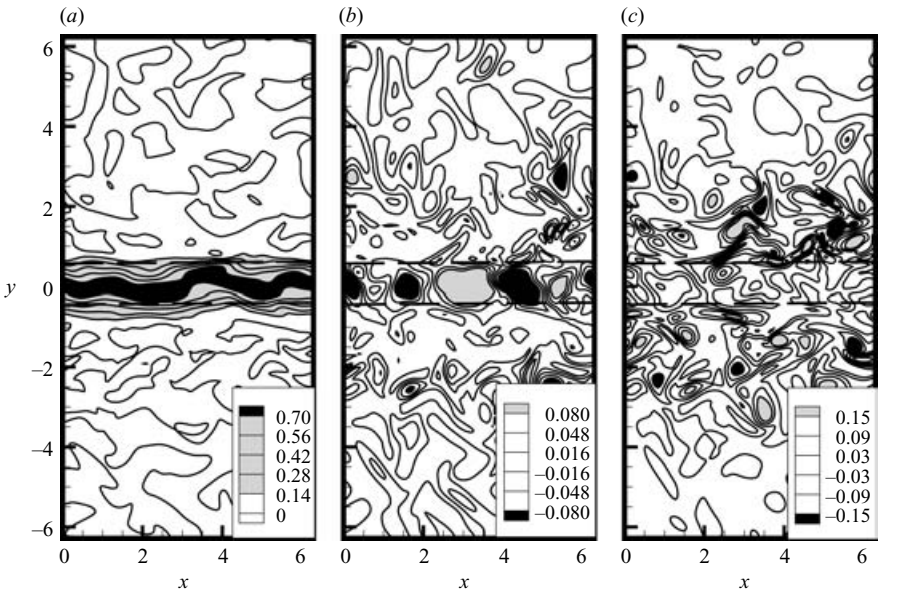


FIGURE 4. Plots showing contours of vorticity components, (*a*) ω_x, (*b*) ω_y, and (*c*) ω_z in a slice of the vortex in the (x, y)-plane, for Case A at $t = 100$.

azimuthal vorticity that join at the loop 'head'. These loops are aligned primarily in the azimuthal direction, but they also have a significant component in the radial direction which arises from the difference in self-induced velocity between the head region and the legs of the vortex loops. A detailed experimental study of this process of entrainment of vortex loops by a columnar vortex is given by Sun & Marshall (2000), and additional information is given in Marshall & Beninati (2000) and Gossler & Marshall (2001).

Contours of the different vorticity components are plotted in figure 4 in an x-y slice of the flow, where the nominal location of the lateral core surface is indicated by dashed lines. The external turbulence induces waves of various types and wavelengths on the vortex core (Bandyopadhay *et al.* 1991; Melander & Hussain 1993*a*; Marshall 1997; Miyazaki & Hunt 2000). While many different wave forms co-exist, the predominant wave observed in the present computations is a bending wave, as can be observed in the contour plots of ω_x and ω_y in figures 4(*a*) and 4(*b*), corresponding to axial vorticity and positive (negative) radial vorticity in the top (bottom) halves of the figure, respectively. The axial vorticity (ω_x) is observed to oscillate in a wavy pattern. The ω_y vorticity component exhibits strong regions of alternating sign at the vortex centre, corresponding to regions where the vortex bending wave crosses the (x, y)-plane. A contour plot of the z-component of vorticity, corresponding to the positive (negative) azimuthal vorticity in the top (bottom) of the plane, is given in figure 4(*c*). The ω_z component has greatest absolute value in the turbulent structures located just outside of the vortex core. Also evident in figure 4(*c*) are long streaks of azimuthal vorticity elongated in the x-direction located just outside the vortex core lateral boundary. These streaks appear to be caused by flattening of the cores of external vortex structures as they are entrained toward the vortex core.

Mean turbulence quantities were obtained by a two-step spatial averaging process. The quantities were first averaged in the axial direction to generate an intermediate

https://doi.org/10.1017/S002211200500580X Published online by Cambridge University Press

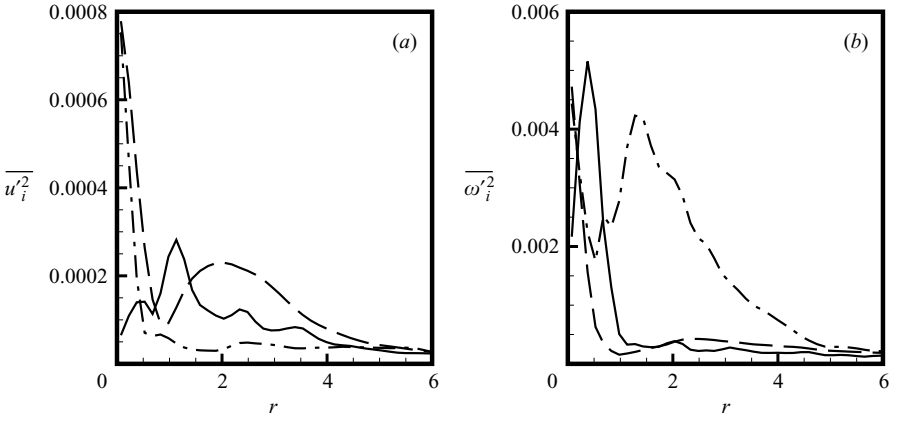


FIGURE 5. Radial variation of (*a*) $\overline{u_x'^2}$ (solid curve), $\overline{u_r'^2}$ (dashed curve), and $\overline{u_\theta'^2}$ (dashed-dotted curve) and (*b*) $\overline{\omega_x'^2}$ (solid curve), $\overline{\omega_r'^2}$ (dashed curve), and $\overline{\omega_\theta'^2}$ (dashed-dotted), for Case A at $t = 100$.

mean, which for some quantity f is given by

$$\overline{\overline{f}}(y, z) \equiv \frac{1}{N_x} \sum_{i=1}^{N_x} f(x_i, y, z). \tag{4}$$

The intermediate averages are then interpolated onto a polar coordinate grid, using 60 evenly spaced bins in the radial direction, and a second azimuthal averaging step is performed to yield the final mean quantity as a function of radial position

$$\overline{f}(r) \equiv \frac{1}{N_\theta} \sum_{j=1}^{N_\theta} \overline{\overline{f}}(r, \theta_j). \tag{5}$$

In these averages, N_x and N_θ denote the number of points in the axial and azimuthal directions, which are set equal to 128 and 64, respectively, in the current computations.

The parts of the turbulent kinetic energy generated by the three velocity components, $\overline{u_x'^2}$, $\overline{u_r'^2}$, and $\overline{u_\theta'^2}$, are plotted in figure 5(*a*) for time $t = 100$, and the corresponding enstrophy perturbations, $\overline{\omega_x'^2}$, $\overline{\omega_r'^2}$, and $\overline{\omega_\theta'^2}$, are plotted in figure 5(*b*). The azimuthally oriented external vortex structures (lying approximately in the interval $1 < r < 3$) induce velocity perturbations primarily in the axial and radial directions, with relatively small velocity perturbations in the azimuthal direction. The bending wave on the central vortex core induces velocity perturbations primarily in the vortex cross-plane (the azimuthal and radial directions), with relatively small induced velocity perturbations in the axial direction. Correspondingly, the axial velocity perturbations and azimuthal vorticity perturbations are strongest in a ring surrounding the vortex core. The radial velocity perturbations exhibit a double-hump, with peaks both in the vortex centre (due to the bending wave on the core) and in a ring surrounding the vortex core (due to the external turbulence). The outer maximum in the radial velocity perturbations is observed to occur at a radius of about $r \cong 2$, whereas the peak in axial velocity perturbations occurs at a radius of about $r \cong 1.2$. The azimuthal velocity perturbations and the radial and axial vorticity perturbations are strongest near the vortex centre, due to the vortex bending waves.

https://doi.org/10.1017/S002211200500580X Published online by Cambridge University Press

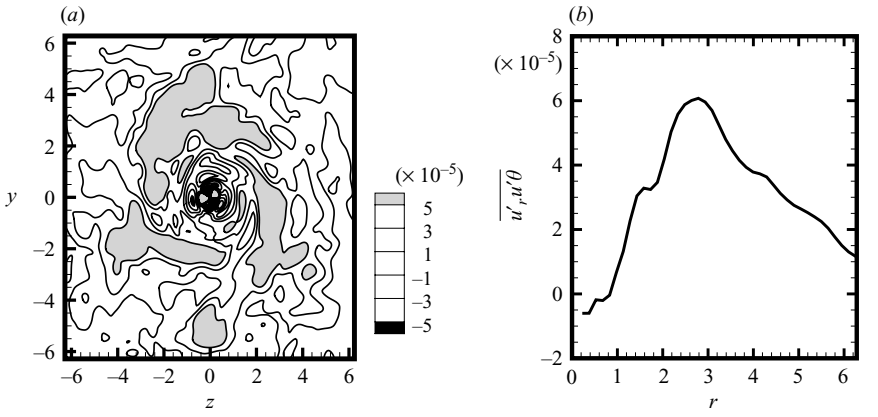


FIGURE 6. Plots showing (*a*) contours of the axially averaged correlation $\overline{\overline{u_r' u_\theta'}}$ in the (y, z)-plane and (*b*) radial variation of $\overline{u_r' u_\theta'}$, for Case A at $t = 100$.

The $\overline{u_r' u_\theta'}$ component of the Reynolds shear stress is responsible for outward momentum transport from the vortex core. Both a contour plot of $\overline{\overline{u_r' u_\theta'}}$ (with axial averaging only) and a line plot of $\overline{u_r' u_\theta'}$ are shown in figure 6. The contour plot exhibits a complex pattern of alternating positive and negative values of $\overline{\overline{u_r' u_\theta'}}$ near the vortex centre, associated with the bending wave on the central vortex core. These positive and negative regions approximately cancel each other out when azimuthally averaged, as indicated by the comparatively small values of $\overline{u_r' u_\theta'}$ within the vortex centre in figure 6(*b*). External to the vortex core there exists a large swath with positive values of $\overline{u_r' u_\theta'}$ due to the mixing induced by the external turbulence structures.

The spectral distribution of the turbulent velocity and vorticity fields is shown in figure 7. In this figure we plot the partial sum of the high-pass-filtered velocity and vorticity components with different values of the cut-off axial wavenumber k_{cut} over a slice of the flow in the (x, y)-plane, given by $\hat{u}_{i,>}^2 \equiv \sum_{k>k_{cut}} \hat{u}_i^2$ and $\hat{\omega}_{i,>}^2 \equiv \sum_{k>k_{cut}} \hat{\omega}_i^2$. The plots utilize values of the cutoff axial wavenumbers of 1, 2, 4 and 6, corresponding to perturbations with wavelength ranging from the vortex core diameter to about six times the core diameter, which is roughly the same as the axial domain size. The various peaks and valleys in these plots correspond to the different flow features discussed in the preceding paragraphs. We focus the present discussion on the spectral content of the various flow features.

The two largest peaks in $\hat{\omega}_{z,>}^2$, centred at about $y = \pm 1.5$, correspond to the external azimuthally aligned turbulence structures, which in turn induce velocity perturbations corresponding to the two large peaks in $\hat{u}_{x,>}^2$ centred at about the same radius and the smaller peaks in $\hat{u}_{y,>}^2$ centred at about $y = \pm 2.4$. The azimuthal vorticity within this external region is dominated by fluctuations with axial wavenumber $k \geqslant 2$, with roughly half of the enstrophy $\hat{\omega}_{z,>}^2$ in the interval $2 \geqslant k \geqslant 4$. By contrast, about half of the kinetic energy due to axial velocity fluctuations, $\hat{u}_{x,>}^2$, in this region have axial wavenumber in the interval $1 \leqslant k \leqslant 2$, with most of the remaining kinetic energy in the interval $2 \geqslant k \geqslant 4$. The radial and axial vorticity components exhibit peaks at about $y = \pm 0.5$ and $y = 0$, respectively, which are due to the presence of the central bending wave on the vortex core. Most of the enstrophy within these peaks is contained in the wavenumber interval $2 \geqslant k \geqslant 4$, and we observe significantly less high-wavenumber enstrophy (e.g. with $k > 6$) here compared to the turbulence in the region external

https://doi.org/10.1017/S002211200500580X Published online by Cambridge University Press

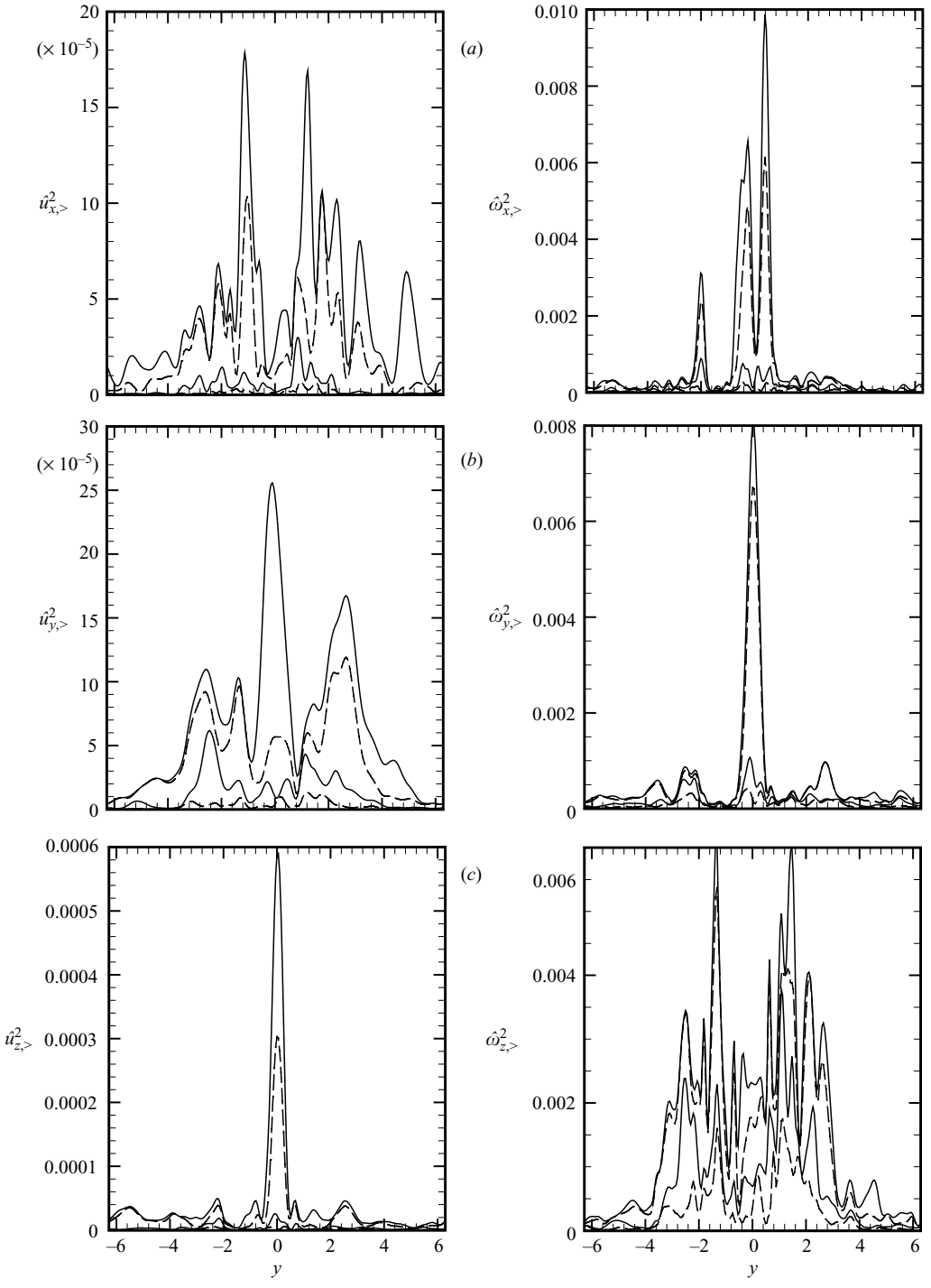


FIGURE 7. Variation of high-pass-filtered turbulence kinetic energy and enstrophy with distance across the vortex core, for (*a*) $\hat{u}^2_{x,>}$ and $\hat{\omega}^2_{x,>}$, (*b*) $\hat{u}^2_{y,>}$ and $\hat{\omega}^2_{y,>}$, and (*c*) $\hat{u}^2_{z,>}$ and $\hat{\omega}^2_{z,>}$, for Case A at $t = 100$. The velocity and vorticity components are high-pass filtered with cutoff axial wavenumbers $k_{cut} = 1$ (upper solid curve), 2 (upper dashed curve), 4 (lower solid curve), and 6 (lower dashed curve).

https://doi.org/10.1017/S002211200500580X Published online by Cambridge University Press

to the vortex core. This wavenumber interval corresponds to waves with length of about 1.5 to 3 times the vortex core diameter, which is in good agreement with the experimental flow visualization results of Bandyopadhyay *et al.* (1991), who report various wave forms on the vortex core in the presence of external turbulence with lengths ranging from 1.06 to 3.1 times the core diameter.

An estimate of the amplitude variation with time of the central bending wave can be obtained by plotting $\hat{\omega}^2_{x,>}$ versus y with $k_{cut} = 1$ over a time interval, as shown in figure 8 at times $t = 40$, 80 and 120. The bending wave amplitude corresponds to the radius at which this curve attains a maximum (or half the distance between the two peaks). Contours of ω_x for the same three times are shown on the left-hand side plots in the figure, and line plots of $\hat{\omega}^2_{x,>}$ versus y with $k_{cut} = 1$ are shown on the right-hand side at the corresponding times. The distances between the peaks in this curve have values 0.5, 0.7, and 0.6 at times 40, 80, and 120, respectively, corresponding to a mean bending wave amplitude of about 0.3. The amplitude of this vortex bending wave appears to remain approximately constant after an initial transient growth period, which is consistent with the RDT predictions of Miyazaki & Hunt (2000).

4. Vorticity transport in external turbulence

The intensity of the external turbulence field is governed by several different physical processes. For instance, we have noted with reference to figure 3 that as the external turbulence loops become oriented in approximately the azimuthal direction, their self-induced velocity acts to entrain them into the vortex core. Different parts of the vortex loops have a larger self-induced velocity than other parts, and hence advect toward the large-scale vortex core faster than other parts of the loop. This difference leads to stretching of the vortex loops due to the differences in mean azimuthal velocity with radial position. Regions of strong enstrophy production rate, $S = \omega_i \omega_j D_{ij}$, where D_{ij} are components of the rate-of-deformation tensor, are plotted using shading in figure 9 for a slice of the flow field in the (x, y)-plane at $t = 100$, with grey shading indicating regions where $S > 0.0004$ and black shading indicating regions where $S < -0.0004$. Contour lines of ω_y, corresponding to the positive (negative) radial vorticity component above (below) the x-axis, are indicated on the same figure using solid (dashed) lines for positive (negative) contours. The strongest enstrophy production occurs within regions of alternating positive and negative sign within the columnar vortex, which are generated by the central bending wave on the large-scale vortex core. Additional regions of (mostly positive) enstrophy generation are found in the turbulence external to the vortex, which are found to correlate closely to contours of radial vorticity.

A potential second mechanism for enhancement of the external turbulence is stripping of vorticity from the large-scale vortex core. This mechanism was observed to play an important role in the turbulence evolution within the vortex core in the flow visualization results of Bandyopadhyay *et al.* (1991) and Sarpkaya & Daly (1987), the latter of which referred to intermittent 'bursts' along the vortex core. A computational study of vortex stripping was reported by Marshall (1997) using an axisymmetric computational model with vortex rings surrounding a columnar vortex. Marshall reports that vortex stripping, typified by a thin ejected vortex sheet from the large-scale vortex core, occurs only for cases with sufficiently strong external vortex rings, the critical strength depending on the ring axial separation and radius. For cases with ring strength below the critical value, a standing wave of variable core area would be set up on the columnar vortex. Since vorticity stripping is accompanied by

https://doi.org/10.1017/S002211200500580X Published online by Cambridge University Press

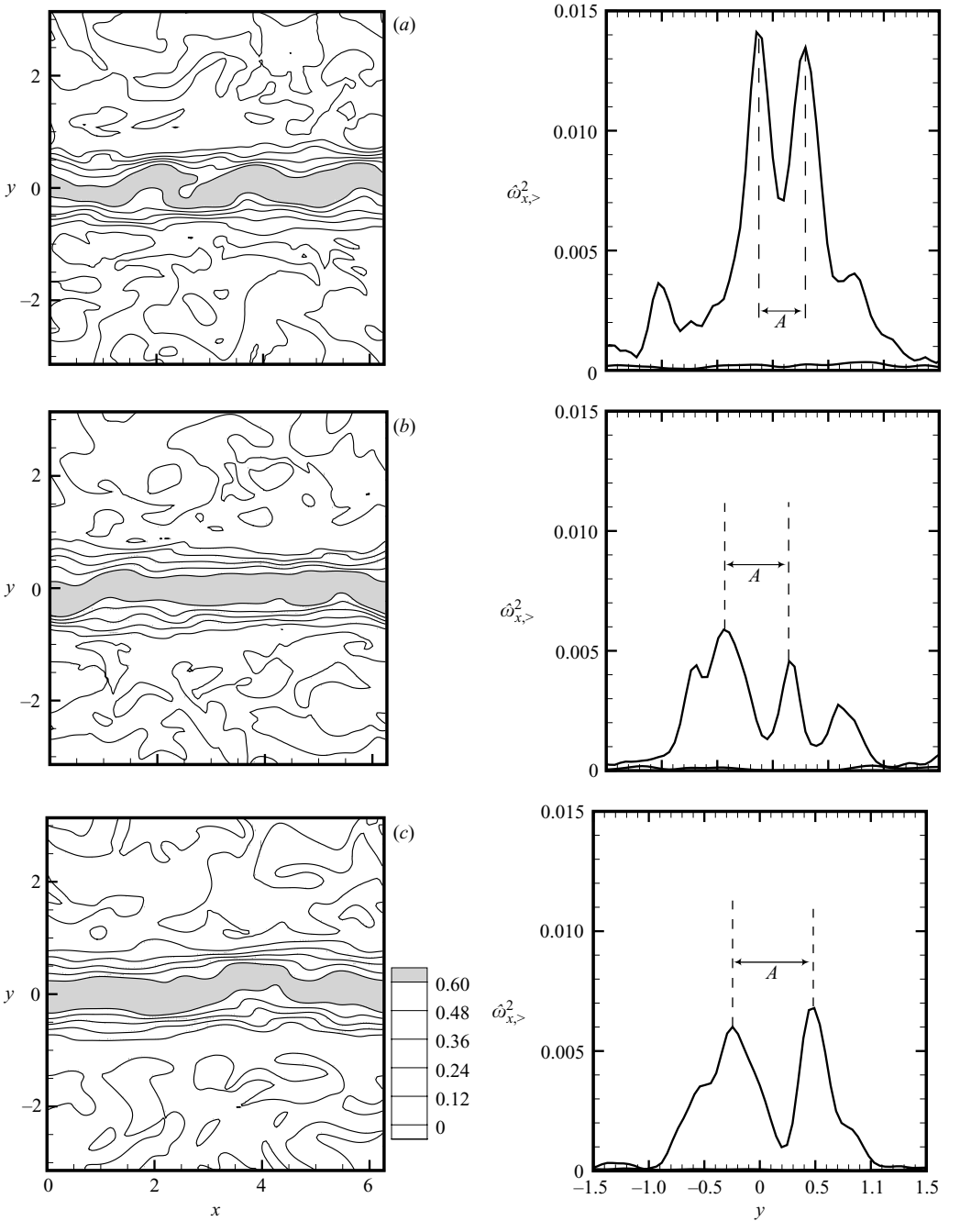


FIGURE 8. Contour plots of ω_x (on the left) and corresponding line plots of $\hat{\omega}^2_{x,>}$ versus y with $k_{cut} = 1$ (on the right) for Case A at times (*a*) $t = 40$, (*b*) $t = 80$, and (*c*) $t = 120$. The distance between the peaks in the figures on the right-hand side is approximately equal to twice the amplitude of the bending wave on the central vortex core.

exchange of fluid from within the large-scale vortex core with that originating outside the core, we examine the extent of vorticity stripping by computing the advection of a passive scalar initiated within the vortex core. The scalar is evolved by the spectral

https://doi.org/10.1017/S002211200500580X Published online by Cambridge University Press

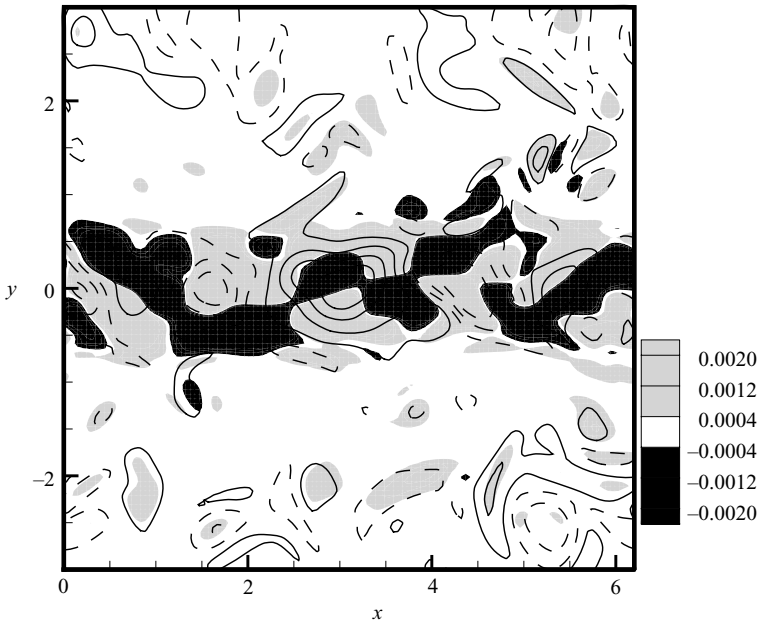


FIGURE 9. Plot showing contours of enstrophy production rate (shading) and ω_y in a slice in the (x, y)-plane for Case A at $t = 100$, where solid lines indicate contours with $\omega_y = 0.0286$, 0.0857, 0.143, and 0.2 and dashed lines indicate contours with $\omega_y = -0.0286$, -0.0857, -0.143, and -0.2.

advection equation, given by

$$\hat{c}^{n+1} = \hat{c}^n - \Delta t \boldsymbol{k} \cdot \left[\tfrac{3}{2}(\widehat{c\boldsymbol{u}})^n - \tfrac{1}{2}(\widehat{c\boldsymbol{u}})^{n-1}\right], \tag{6}$$

where c is the scalar concentration, a hat denotes Fourier transform, and the second-order Adams–Bashforth method is used for time stepping. In various tests, the scalar is observed to advect with the fluid flow with no dissipation and no detectible spurious oscillations. The scalar concentration field is initiated within the vortex core at the end of the initialization run (following Step 8, described in § 2) using the distribution

$$c(r) = 1 - \exp\left[-\frac{\ln(2)e^2}{3r}\exp\left(\frac{1}{1.5r - 1}\right)\right]. \tag{7}$$

This distribution is similar to a top-hat function with radius $r = 0.5$, but has somewhat more gradual variation near the sides to avoid Gibbs oscillations. Plots of the passive scalar at different times for cases with moderate turbulence initial intensity (e.g. Cases A–D) exhibit waves of various types on the vortex core, but no ejection of the core fluid out into the external flow, indicating that vortex stripping does not have a significant effect on the external turbulence for these cases. (Cases with strong initial turbulence are examined later in § 6.) One reason for the difference between this result and the observations of Bandyopadhyay *et al.* (1991) and Sarpkaya & Daly (1987) may be that the vortex Reynolds number (based on the definition $Re_V \equiv \Gamma/\nu$ used in the current paper) is in the range 10 000–60 000 for Sarpkaya & Daly (1987) and 94 000–157 000 for Bandyopadhyay *et al.* (1991), which in both cases is substantially higher than in the current paper (for which $Re_V = 3000$). Also, Sarpkaya & Daly's work was for a vortex pair, for which Devenport, Zsolodos & Vogel (1997) and

https://doi.org/10.1017/S002211200500580X Published online by Cambridge University Press

Risso *et al.* (1997) report that stretching from the opposing vortex of the pair can substantially enhance the vortex turbulence.

A variety of processes act to suppress the external turbulence, including viscous diffusion, merger of external vortex structures of the same-sign azimuthal vorticity, and outward propagation of pairs of vortex structures with opposite-sign azimuthal vorticity arising from two different vortex loops. The latter process increases dispersion of turbulence and opposes the vortex loop entrainment process. Of these various processes, the average core size of individual external vortex structures in the current computations appears to be most affected by stretching and viscous diffusion. If R denotes the average radial position of a vortex loop located outside of the columnar vortex core, we estimate that the difference in radial distance between the 'head' region and the legs of a vortex loop is approximately $\Delta R \cong (\pi R^2/\delta)(\Gamma_L/\Gamma)$, where δ is the average distance between the legs of a vortex loop and Γ_L denotes the typical strength of an external vortex loop (Beninati 2004). The associated stretching rate of the vortex loop is $S \cong \Gamma\,\Delta R/4\pi^2R^2$. Using the classical Burger's (1948) vortex solution for an equilibrium stretched vortex, the last two results yield an expression for the typical core radius, a_L, of an external turbulent vortex structure as

$$a_L = \sqrt{2\nu/S} \cong \left[\frac{8\pi\nu R\delta}{\Gamma_L}\right]^{1/2}. \tag{8}$$

Assuming now that δ and R are proportional to a_L and core radius a of the columnar vortex, respectively, such that $\delta = c_1 a_L$ and $R = c_2 a$, and writing the circulation in terms of the maximum axial vorticity $\omega_{x,\max}$ in the columnar vortex and the maximum azimuthal vorticity $\omega_{\theta,\max}$ in the external turbulence as $\Gamma = \pi a^2 \omega_{x,\max}$ and $\Gamma_L = \pi a_L^2 \omega_{\theta,\max}$, the result (8) can be written as

$$\frac{a_L}{a} \cong \left(\frac{C}{Re_V}\frac{\omega_{x,\max}}{\omega_{\theta,\max}}\right)^{1/3}, \tag{9}$$

where $C \equiv 8\pi c_1 c_2$ is a constant. Our computational results for Case A at $t \cong 100$, for instance, yield $\omega_{x,\max}/\omega_{\theta,\max} \cong 5$, $c_1 \cong 4$, and $c_2 \cong 2$, such that $C \cong 200$ and the core radius of the external turbulence structures is estimated to have equilibrium length scale $a_L \cong 0.7a$.

5. Proper-orthogonal decomposition analysis

Proper-orthogonal decomposition (POD) provides a method for extracting the most energetic modes of a turbulent flow at different wavenumbers (Lumley 1967; Holmes, Lumley & Berkooz 1996). We employ a simplified POD procedure related to the 'slice POD' approach described by Gamard *et al.* (2002) with application to a statistically stationary, spatially developing, axisymmetric jet flow. Since the flow considered in the current study is periodic in the axial direction and decaying in time, we evaluate the POD using a fixed time and the Fourier-transformed velocity field in the axial and azimuthal directions. The slice POD is obtained by expanding a scalar function $u(t, r; m, k)$ about a set of orthogonal eigenfunctions $\phi^{(n)}(t, r; m, k)$ as

$$u(t, r; m, k) = \sum_{n=1}^{\infty} a_n(t; m, k)\phi^{(n)}(t, r; m, k), \tag{10}$$

where m and k represent the azimuthal and axial wavenumbers, respectively, and u denotes the Fourier transform in the (θ, x)-plane of a scalar function or the component

https://doi.org/10.1017/S002211200500580X Published online by Cambridge University Press

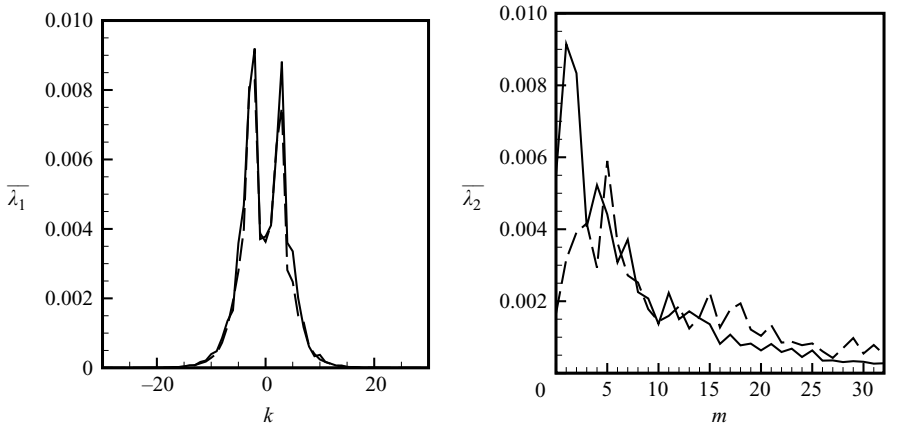


FIGURE 10. Plot of the POD eigenvalues of the azimuthal vorticity component (solid curve) and radial vorticity component (dashed curve) at time $t = 100$ for Case A. The eigenvalues are summed over all azimuthal wavenumbers in (*a*) and over all axial wavenumbers in (*b*).

of a vector. The integral equation for the POD eigenfunctions is given by (Gamard *et al.* 2002)

$$2\pi \int_0^\infty R(t, r, r'; m, k)\phi^{(n)}(t, r'; m, k) r' \, \mathrm{d}r' = \lambda^{(n)}\phi^{(n)}(t, r; m, k), \tag{11}$$

where $R(t, r, r'; m, k) \equiv u(t, r; m, k)u(t, r'; m, k)$ and $\lambda^{(n)}$ are the POD eigenvalues. It is convenient for numerical solution of (11) to make the kernel symmetric by defining new eigenfunctions $\psi^{(n)} \equiv r^{1/2}\phi^{(n)}$, such that

$$2\pi \int_0^\infty \left[r^{1/2} R(t, r, r'; m, k)(r')^{1/2}\right] \psi^{(n)}(t, r'; m, k) \, \mathrm{d}r' = \lambda^{(n)}\psi^{(n)}(t, r; m, k). \tag{12}$$

The POD provides a method to compare the energy contained in different functions describing the turbulent flow by comparing the first eigenvalue, or the sum of the first few eigenvalues, for the corresponding m and k values. The POD eigenvalues are computed in the current computations by first interpolating the computational velocity and vorticity fields from the original Cartesian grid to a cylindrical polar grid, taking the discrete Fourier transform in the azimuthal and axial directions, discretizing the integral over r in (12), and solving for the first few eigenvalues of the resulting algebraic eigenvalue problem for each m and k value using the DSYEVX subroutine in the LAPACK package.

We utilize the POD method by examining the spectral content of the turbulence and the vortex response for a specific case with external turbulence magnification factor $f_{magn} = 1$ (Case A) by plotting the POD eigenvalues for different values of the axial and azimuthal wavenumbers, k and m, respectively. Unlike the usual Fourier spectrum, the POD eigenvalue contains spectral information from the entire flow, but weights that information based on the most energetic regions of the flow. By summing the POD eigenvalues over either the axial or azimuthal wavenumbers, we can examine how the energy is distributed with regard to the other wavenumber. For example, the POD eigenvalues of the radial and azimuthal vorticity components for the turbulent vortex are summed over all azimuthal wavenumbers, e.g. $\bar{\lambda}_1(k) \equiv \sum_m \lambda_{\omega_\theta}(k, m)$, and plotted as a function of axial wavenumber in figure 10. Such plots provide a concise method for interpreting the spectral content of the different components of the vorticity field. For

https://doi.org/10.1017/S002211200500580X Published online by Cambridge University Press

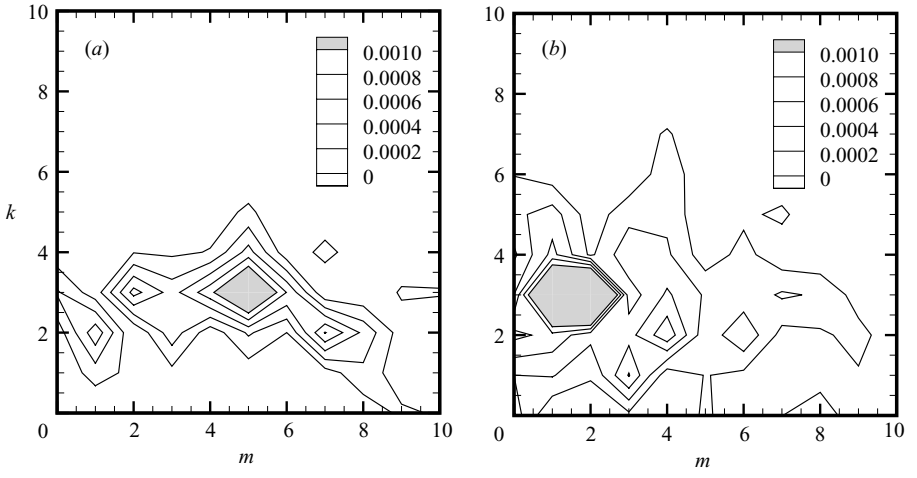


FIGURE 11. Contour plot of POD eigenvalues for (*a*) radial and (*b*) azimuthal vorticity components at time $t = 100$ for Case A.

instance, in figure 10(*a*) we see that the radial and azimuthal vorticity are contained mostly in turbulent structures with axial wavenumber $|k| \leqslant 10$, peaking at an axial wavenumber of about 3. In figure 10(*b*), these same vorticity components are summed over all axial wavenumbers, e.g. $\bar{\lambda}_2(m) \equiv \sum_k \lambda_{\omega_\theta}(k, m)$, and plotted as a function of azimuthal wavenumber. The radial vorticity has peaks at $m = 3$ and $m = 5$, and then decays significantly for high azimuthal wavenumbers. Most of the contributions to the azimuthal vorticity components are in the range $m < 10$, including large values for $m = 0$ and $m = 1$, corresponding to nearly axisymmetric external turbulence and the bending wave on the central vortex core, respectively.

The POD eigenvalues for the radial and azimuthal vorticity components are plotted as a function of wavenumbers m and k in figure 11. A local maximum in the radial vorticity occurs for $(m, k) = (5, 3)$, which is related to the spots of radial vorticity near the centre of the vortex core caused by the central bending wave, as shown in figure 4(*b*). The azimuthal vorticity eigenvalue (associated primarily with the external turbulence) has large values in a broader region corresponding to $2 \leqslant k \leqslant 4$ and $0 \leqslant m \leqslant 3$.

6. Effect of external turbulence initial condition

The external turbulence can be characterized by an initial length scale and kinetic energy distribution. In this section, we compare computations in which the initial length scale and turbulent kinetic energy profile are different to examine the effect of the turbulence initial condition on the turbulence state and the turbulence–vortex interaction.

6.1. *Effect of initial turbulence length scale*

The first set of computations compares two cases in which the initial homogeneous turbulence has very different length scales (Cases A and B), both with magnification factor $f_{magn} = 1$. In Case A, the truncation wavenumbers k_1 and k_2 in Step 1 of the initiation procedure are set to 10 and 30, respectively, whereas in Case B we examine larger-scale initial perturbations with the wavenumber truncation limits 5 and 10, respectively. The initial root-mean-square velocity perturbation amplitude is set the same

https://doi.org/10.1017/S002211200500580X Published online by Cambridge University Press

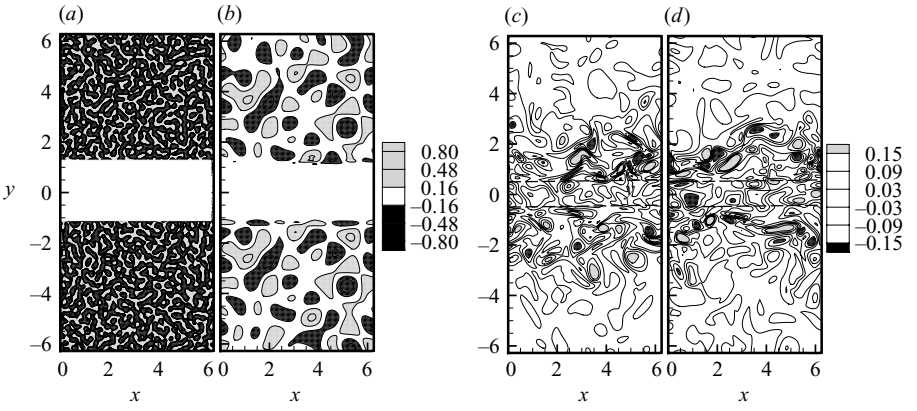


FIGURE 12. Comparison of azimuthal vorticity contours for two computations with different initial turbulence length scales (Cases A and B). Plots (*a*) and (*b*) are at the beginning of the initialization run and (*c*) and (*d*) are at time $t = 100$ of the final run, where (*a*) and (*c*) for Case A and (*b*) and (*d*) for Case B.

for both cases. Contour plots showing the azimuthal vorticity field both for a time corresponding to the end of Step 2 of the initialization procedure described in § 2 ($t = 0$ of the initialization run) and at $t = 100$ (of the final run) are shown in figure 12. The initial length scale is clearly much shorter for Case A than it is for Case B; however, by time $t = 100$ the turbulence length scale appears visually to be similar for the two cases.

A more quantitative method of examining the variation in axial length scales of the external turbulence is to plot the enstrophy component $\overline{\omega_\theta'^2}$ associated with the azimuthal vorticity as a function of radius, as shown in figure 13. Figures 13(*a*) and 13(*b*) correspond to times $t_{init} = 0$ and 20 of the initialization run and figures 13(*c*) and 13(*d*) correspond to times $t = 0$ and 100 of the final run. In figure 13(*a*), the computation with smaller axial length scales (and hence larger wavenumber range) has much larger azimuthal vorticity magnitudes in order to achieve the same velocity fluctuation magnitudes as the case with larger axial length scales. The magnitude of $\overline{\omega_\theta'^2}$ outside of the vortex core differs in the two cases by a factor of about 500 in figure 13(*a*). In figure 13(*b*), the strength of the vortex structures in Case A has decreased markedly. By the end of the initiation run (figure 13*c*), the enstrophy far away from the vortex core is similar for the two cases, due to decay of much of the initial high-wavenumber components of the turbulent flow. By time $t = 100$ of the final run (figure 13*d*), the enstrophy profiles for the two cases are nearly identical.

6.2. *Effect of initial turbulence intensity*

We have performed computations with several different values of the external turbulence intensity by adjusting the turbulence magnification value f_{magn} in Step 6 of the initiation procedure, with all other features of the initial condition the same. The qualitative nature of the turbulence–vortex interaction is the same for all cases examined, but the rate at which the flow advances through the turbulence decay process differs. In figure 14 we compare enstrophy $\overline{\omega_\theta'^2}$ associated with the azimuthal vorticity perturbation for cases with $f_{magn} = 0.5$ and 2 (Cases C and D), evaluated at times $t = 0$, 40, 80, 120 and 160. Since $\overline{\omega_\theta'^2}$ is dominated by the wrapped external vortex structures, the plot of $\overline{\omega_\theta'^2}$ versus r exhibits a peak in the interval $1 < r < 2$. A second peak in $\overline{\omega_\theta'^2}$ occurs near the origin due to the bending wave on the large-scale vortex core.

https://doi.org/10.1017/S002211200500580X Published online by Cambridge University Press

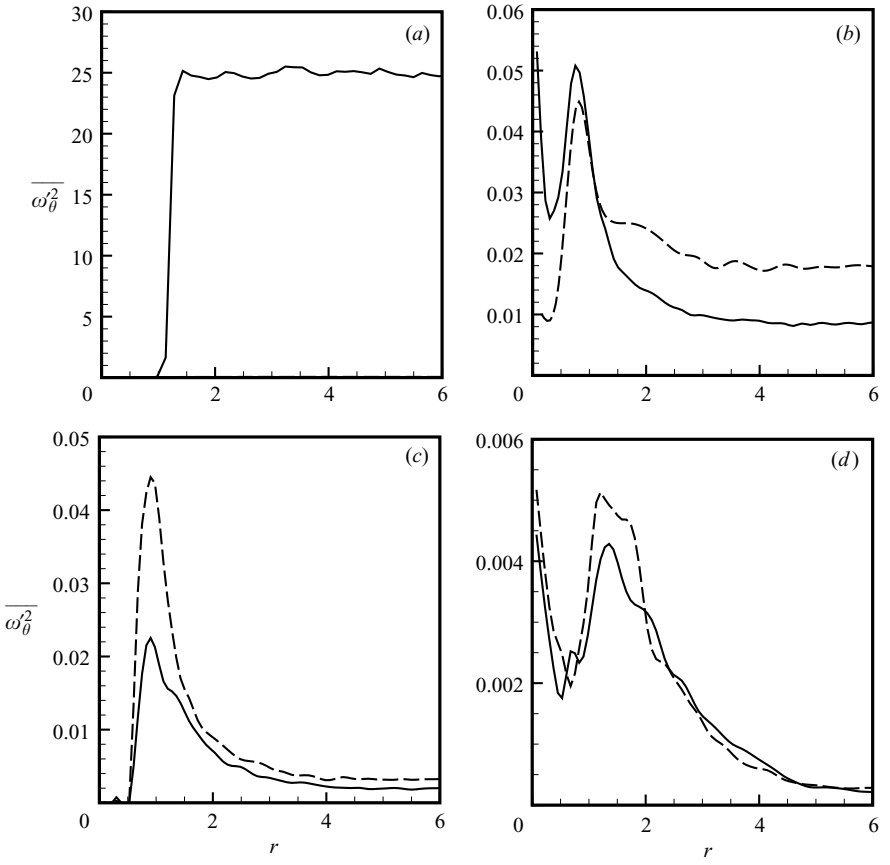


FIGURE 13. Comparison of $\overline{\omega_\theta'^2}$ versus radial distance for cases with two different initial length scales, Case A (solid curve) and Case B (dashed curve). Plots are given for times (*a*) $t=0$ of the initialization run, (*b*) $t=20$ of the initialization run, (*c*) $t=0$ of the final run, and (*d*) $t=100$ of the final run. In (*a*), the maximum magnitude for Case B (not visible on the figure) is about 500 times less than that for Case A.

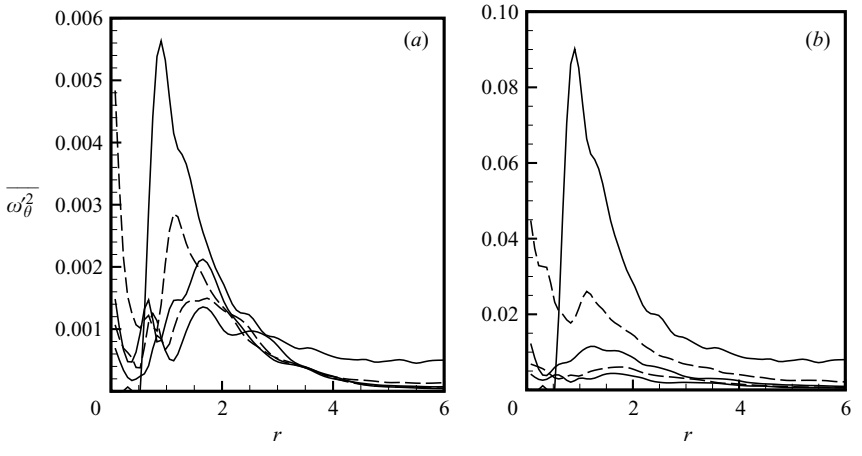


FIGURE 14. Comparison of $\overline{\omega_\theta'^2}$ variation with r in computations with (*a*) $f_{magn}=0.5$ (Case C) and (*b*) $f_{magn}=2$ (Case D), showing results (from top to bottom) at times $t=0$ (top solid curve), 40 (dashed curve), 80 (solid curve), 120 (dashed curve), and 160 (bottom solid curve).

https://doi.org/10.1017/S002211200500580X Published online by Cambridge University Press

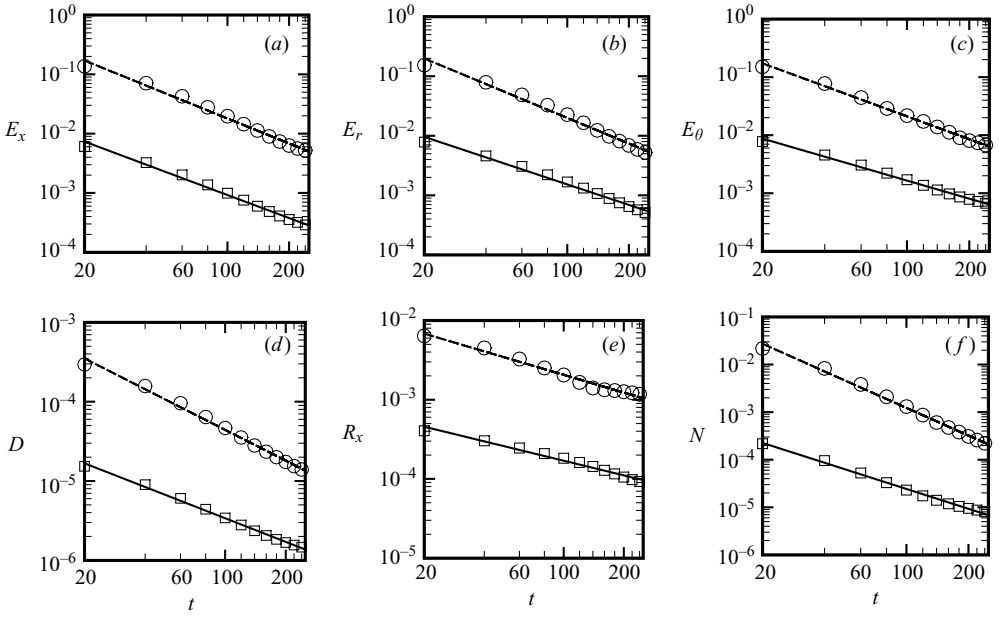


FIGURE 15. Log–log plots showing decay with time of enstrophy perturbation measures (*a*) E_x, (*b*) E_r, (*c*) E_θ, (*d*) D, (*e*) R_x, and (*f*) N. Circles and the dashed line are for Case D, and squares and the solid line are for Case C.

Case	E_x	E_r	E_θ	D	R_x	N
C	−1.29	−1.14	−1.03	−0.99	−0.61	−1.38
D	−1.40	−1.43	−1.31	−1.29	−0.74	−1.93

TABLE 2. Slopes for various integral quantities when plotted versus time on a log–log plot, for Cases C and D.

At the initial time, all of the different cases exhibit similar $\overline{\omega_\theta'^2}$ profiles, with the maximum values scaling as f_{magn}^2, such that the peak value for the $f_{magn}=2$ case is about 16 times the peak value for the $f_{magn}=0.5$ case. The value of $\overline{\omega_\theta'^2}$ decays with time for both cases. In order to quantify the vorticity decay in time, we have integrated each component of the enstrophy over the vortex cross-section to form the integral enstrophy measures

$$E_x \equiv 2\pi \int_0^{2\pi} \overline{\omega_x'^2} r \, \mathrm{d}r, \quad E_r \equiv 2\pi \int_0^{2\pi} \overline{\omega_r'^2} r \, \mathrm{d}r, \quad E_\theta \equiv 2\pi \int_0^{2\pi} \overline{\omega_\theta'^2} r \, \mathrm{d}r. \tag{13}$$

These enstrophy measures are observed to decay linearly in time on a log–log plot (figure 15), with slope s given in table 2, implying that there exists a power-law decay in time of the form $E_\theta(t) = E_\theta(0) t^{-s}$ (and similarly for the other quantities listed in table 2). We also observe that the integral over the dissipation rate, the energy associated with the axial velocity component, and the enstrophy production rate, given by

$$D \equiv 2\pi \int_0^{2\pi} 2\nu \overline{D_{ij} D_{ij}} r \, \mathrm{d}r, \quad R_x \equiv 2\pi \int_0^{2\pi} \overline{u_x'^2} r \, \mathrm{d}r, \quad N \equiv 2\pi \int_0^{2\pi} \overline{\omega_i D_{ij} \omega_j} r \, \mathrm{d}r, \tag{14}$$

decay linearly in time when plotted on a log–log plot.

https://doi.org/10.1017/S002211200500580X Published online by Cambridge University Press

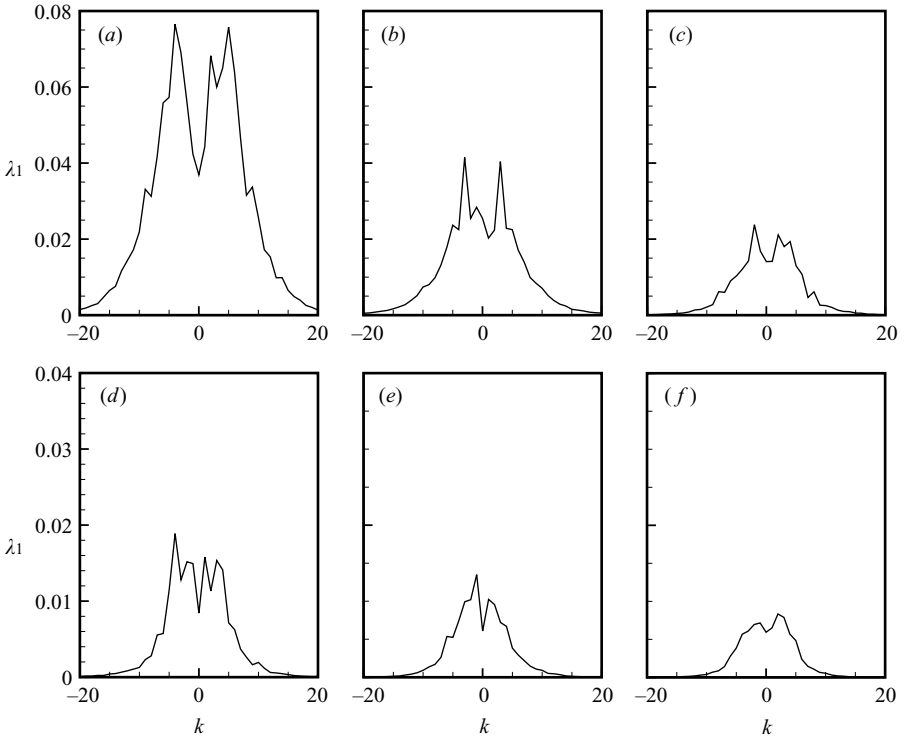


FIGURE 16. POD eigenvalues summed over azimuthal wavenumbers for Case D at times (*a*) $t = 0$, (*b*) 40, (*c*) 80, (*d*) 120, and (*e*) 160.

Some of the quantities in (13) and (14) can be related using the global kinetic energy conservation law for flow in a periodic space, given by (Frisch 1995)

$$\frac{\mathrm{d}}{\mathrm{d}t}\left\langle \frac{1}{2}q^2 \right\rangle = -2\nu\langle D_{ij}D_{ij}\rangle = -\nu\langle\omega^2\rangle, \tag{15}$$

where q^2 is the velocity magnitude squared and angle brackets denote an average over the flow domain. Using the Reynolds decomposition, (15) can be rewritten as

$$\frac{\mathrm{d}}{\mathrm{d}t}(R + R_r + R_\theta + R_x) = -2D = -\nu(E + E_r + E_\theta + E_x), \tag{16}$$

where R and E are the integrals of the mean velocity magnitude squared, $\bar{u}^2$, and the mean vorticity magnitude squared, $\bar{\omega}^2$, respectively, over the vortex cross-section. While E_r and E_x are dominated by perturbations on the large-scale vortex, E_θ and D are dominated by the external turbulence. It is therefore of interest to note the close correspondence in the slopes given in table 2 for E_θ and D. Equation (16) also suggests that if s is the slope of the enstrophy decay curve, then R_x should decay with slope $s-1$; however, table 2 gives a somewhat larger value for the decay slope of this term. We note that the other energy terms, R, R_r and R_θ, do not appear to decay with time via a power-law expression, so it is difficult to estimate the effect of these terms.

The time variation of length scale of the external turbulence can be examined by plotting the POD eigenvalues of the azimuthal vorticity component, summed over all azimuthal wavenumbers, as a function of the axial wavenumber, which

https://doi.org/10.1017/S002211200500580X Published online by Cambridge University Press

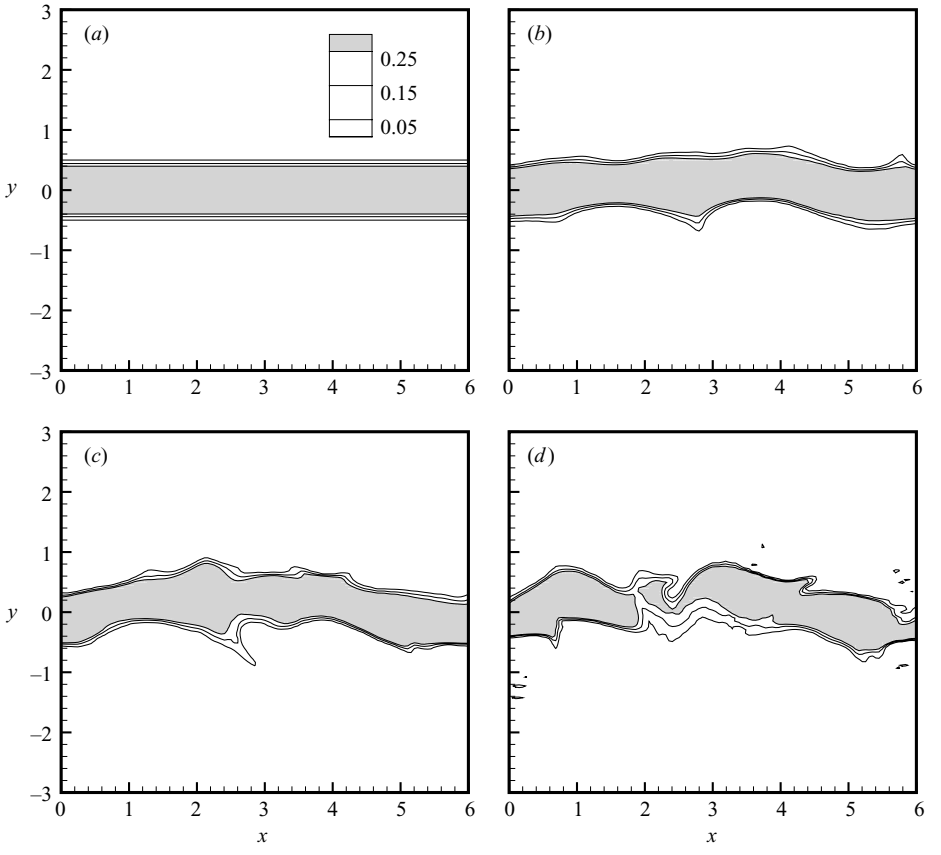


FIGURE 17. Contour plots of the passive scalar concentration for Case E at times (*a*) $t = 0$, (*b*) 5, (*c*) 10, and (*d*) 15.

is given in figure 16 for a case with $f_{magn} = 2$ (Case D). A gradual decrease in magnitude of the POD eigenvalue is observed, associated with decay of E_θ in time. As would be expected, we also observe that enstrophy at higher wavenumbers dies out more quickly, leading to a progressively narrowing band of axial wavenumbers with significant POD eigenvalues in figure 16.

6.3. *Turbulence-induced vortex breakup*

Sufficient magnification of the external turbulence can lead to breakup of the large-scale vortex core. This breakup process is illustrated for a case with $f_{magn} = 3$ (Case E) by plotting contours of the passive scalar concentration over a time series in figure 17, where the passive scalar is used to identify fluid originating within the vortex core. We first observe waviness of the core boundary for short time, followed by ejection of the core fluid via a vorticity stripping process (figure 17*c*). As the external turbulence continues to entrain into the core, we observe large-scale breakup of the core fluid into multiple pieces. As noted previously, it is likely that the vorticity stripping process would be dominant for a longer period of time and for a wider range of external turbulence magnitudes for cases at higher Reynolds numbers.

The dependence of the vortex breakup on the value of f_{magn} is examined in figure 18 by plotting the contours of the passive scalar used to mark the core fluid in a slice

https://doi.org/10.1017/S002211200500580X Published online by Cambridge University Press

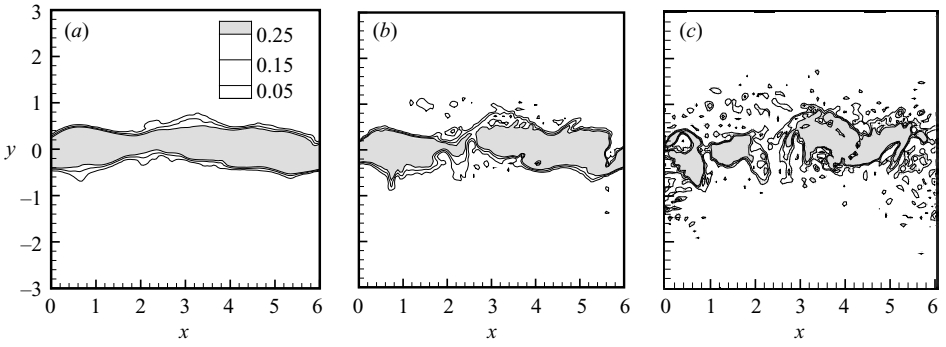


FIGURE 18. Comparison of contour plots of passive scalar concentration at time $t = 20$ for (*a*) $f_{magn} = 2$ (Case D), (*b*) $f_{magn} = 3$ (Case E), and (*c*) $f_{magn} = 4$ (Case F).

of the flow in the (x, y)-plane for $f_{magn} = 2$, 3 and 4 (Cases D–F) at time $t = 20$. For $f_{magn} = 2$, the passive scalar has a wavy shape, but it maintains a connected tube-like form within the core. For $f_{magn} = 3$, the passive scalar both begins to break up into multiple segments and exhibits shedding in thin sheets from the central core. For $f_{magn} = 4$, we observe breakup of the passive scalar into numerous segments and numerous ejections of the scalar in thin sheets into the external fluid all around the lateral surface of the larger segments.

7. Conclusions

This paper reports results of a study using spectral DNS and proper-orthogonal decomposition to examine the interaction between an initially columnar vortex and external turbulence. Although the computations are performed in a domain with periodic boundary conditions, the lateral spacing between the vortices is taken as large enough to approximate an isolated vortex. A multi-step initialization procedure is employed in order to develop an initial turbulence field that possesses the wrapped, nearly axisymmetric form characteristic of vortex turbulence. Cases with various values of the external turbulence intensity and length scale are examined.

The external turbulence wraps around the large-scale vortex and forms loop structures that are oriented primarily in the azimuthal direction. Different parts of these loop structures become entrained into the vortex core at different rates, which gives rise to a non-zero radial vorticity component, and associated vortex stretching, in the external turbulence. As the external vortex loops advect close to the large-scale vortex core, the cross-section of the vortex loops becomes elongated in the axial direction. The external turbulence exhibits a broad band of axial wavelengths, which grows progressively more focused on the larger wavelengths as time progresses. For most of the current computations, the enstrophy within the external turbulence is contained in axial wavelengths greater than about half the large-scale vortex core diameter, with the mode with greatest enstrophy corresponding to about twice the core diameter.

The large-scale vortex responds to external turbulence of moderate strength by formation of a wide variety of wave forms; however, of these the bending wave is the most prominent. The turbulent kinetic energy and enstrophy profiles thus exhibit two peaks: one within the external turbulence at about 1–3 core diameters from

https://doi.org/10.1017/S002211200500580X Published online by Cambridge University Press

the vortex centre and one at the large-scale vortex centre, where the latter is caused by buffeting of the large-scale vortex by the external turbulence. Once the vortex bending wave forms, its amplitude does not seem to continue growing in time. The dominant wavelength of the bending wave appears to be about twice the vortex core diameter, which compares well with the experimental flow visualization results of Bandyopadhyay *et al.* (1991). There appears to be little stripping of vorticity from the vortex core for the relatively low Reynolds number used in the current computations for initial turbulence of moderate strength.

Computations performed with different initial turbulence length scales indicate that the turbulence approaches a similar length scale as the computation progresses. Computations are performed with a wide range of different turbulence intensities. For all cases with moderate turbulence strength, the different components of the turbulence enstrophy, the dissipation rate, the enstrophy production rate, and the axial turbulence kinetic energy are observed to decrease in time via a power-law expression, where the power-law exponent depends only slightly on the turbulence intensity. At sufficiently high initial turbulence intensity, the external turbulence is observed to induce breakup of the large-scale vortex core. This breakup is initiated by stripping of vorticity from the lateral surface of the vortex core, followed by wholesale breakup of the core.

A number of aspects of the turbulent vortex problem require further clarification in a future study. The effect of significantly higher Reynolds number is of particular interest, since experimental data for high-Reynolds-number vortices immersed in turbulent surroundings indicate the presence of significant stripping of the outer parts of the vortex, which are ejected out into the external turbulence. This stripping mechanism was not prominent in the current computations, except just prior to breakup of the large-scale vortex. A second matter for future study is the effect of straining in the vortex cross-sectional plane on the turbulence, as might be caused by nearby parallel large-scale vortices. Whereas the present computations exhibit steadily decaying turbulent energy, the presence of an imposed straining might introduce sufficient stretching of the turbulence structures to halt the turbulence decay. This supposition is supported by the significant increase in turbulence intensity for a vortex pair (compared to a single vortex) observed in the experiments of Devenport *et al.* (1997), as well as by our own preliminary computations.

Note Added in Proof: After acceptance of this paper, we became aware of the interesting study by Pradeep & Hussain (2004), which showed that periodic lateral boundary conditions used in flows with non-zero vortex circulation can, at sufficiently high Reynolds numbers, give rise to a centrifugal instability that for turbulence–vortex interaction studies leads to artificial growth of the turbulence external to the vortex. In preliminary computations with domain spanning the interval $(-\pi, \pi)$ in the y- and z-directions, we did indeed observe spurious turbulence growth of the type described by Pradeep & Hussain. However, when the domain size is increased to the value $(-2\pi, 2\pi)$ in the y- and z-directions used in the current paper, such that the vortex occupies only 0.5% of the domain cross-sectional area, the external turbulence monotonically decays according to a power law (figure 15) over the time interval examined in the computations and no spurious turbulence growth is observed. We therefore feel that the computations presented in the paper are not significantly influenced by the numerical instability described by Pradeep and Hussain, although we concur with their recommendation for use of alternative numerical methods for future studies.

https://doi.org/10.1017/S002211200500580X Published online by Cambridge University Press

Research support for M. L. B. was provided by the Iowa Presidential Fellowship Program, by the American Association of University Women sponsored Dissertation Fellowships and by IIHR – Hydroscience and Engineering. Computer time for this work was provided by a grant from the National Partnership for Advanced Computational Infrastructure, San Diego, California.

REFERENCES

Bandyopadhyay, P. R., Stead, D. J. & Ash, R. L. 1991 Organized nature of a turbulent trailing vortex. *AIAA J.* **29**, 1627–1633.

Beninati, M. L. 2004 External turbulence interaction with a columnar vortex. PhD disseration, University of Iowa.

Beninati, M. L. & Marshall, J. S. 2005 An experimental study of the effect of free-stream turbulence on a trailing vortex. *Exps. Fluids* **38**, 244–257.

Bradshaw, P. 1969 The analogy between streamline curvature and buoyancy in turbulent shear flow. *J. Fluid Mech.* **36**, 177–191.

Burgers, J. M. 1948 A mathematical model illustrating the theory of turbulence. *Adv. Appl. Mech.* **1**, 171–199.

Crow, S. C. 1970 Stability theory for a pair of trailing vortices. *AIAA J.* **8**, 2172–2179.

Devenport, W. J., Zsolodos, J. S. & Vogel, C. M. 1997 The structure and development of a counter-rotating wing-tip vortex pair. *J. Fluid Mech.* **332**, 71–104.

Frisch, U. 1995 *Turbulence*, pp. 18–21. Cambridge University Press.

Gamard, S., George, W. K., Jung, D. & Woodward, S. 2002 Application of a 'slice' proper orthogonal decomposition to the far field of an axisymmetric turbulent jet. *Phys. Fluids* **14**, 2515–2522.

Gossler, A. A. & Marshall, J. S. 2001 Simulation of normal vortex-cylinder interaction in a viscous fluid. *J. Fluid Mech.* **431**, 371–405.

Holmes, P., Lumley, J. L. & Berkooz, G. 1996 *Turbulence, Coherent Structures, Dynamical Systems and Symmetry*. Cambridge University Press.

Krishnamoorthy, S. & Marshall, J. S. 1998 Three-dimensional blade-vortex interaction in the strong-vortex regime. *Phys. Fluids* **10**, 2828–2845.

Lessen, M., Singh, P. J. & Paillet, F. 1974 The instability of a trailing line vortex. Part 1. Inviscid theory. *J. Fluid Mech.* **63**, 753–763.

Liu, H. T. 1992 Effects of ambient turbulence on the decay of a trailing vortex wake. *J. Aircraft* **29**, 255–263.

Lumley, J. L. 1967 The structure of inhomogeneous turbulence. In *Atmospheric Turbulence and Wave Propagation* (ed. A. M. Yaglom & V. I. Tatarski), pp. 166–178. Nauka, Moscow.

Marshall, J. S. 1997 The flow induced by periodic vortex rings wrapped around a columnar vortex core. *J. Fluid Mech.* **345**, 1–30.

Marshall, J. S. 2003 Cross-stream vorticity field induced by streamwise vortices in unbounded and wall-bounded shear flows. *Theor. Comput. Fluid Dyn.* **16**, 231–247.

Marshall, J. S. & Beninati, M. L. 2000 Turbulence evolution in vortex-dominated flows. In *Nonlinear Instability, Chaos and Turbulence* II (ed. L. Debnath & D. N. Riahi), pp. 1–40. WIT Press.

Melander, M. V. & Hussain, F. 1993*a* Coupling between a coherent structure and fine-scale turbulence. *Phys. Rev.* E **48**, 2669–2689.

Melander, M. V. & Hussain, F. 1993*b* Polarized vorticity dynamics on a vortex column. *Phys. Fluids* **5**, 1992–2003.

Miyazaki, T. & Hunt, J. C. R. 2000 Linear and nonlinear interactions between a columnar vortex and external turbulence. *J. Fluid Mech.* **402**, 349–378.

Pradeep, D. S. & Hussain, F. 2004 Effects of boundary condition in numerical simulations of vortex dynamics. *J. Fluid Mech.* **516**, 115–124.

Risso, F., Corjon, A. & Stoessel, A. 1997 Direct numerical simulations of wake vortices in intense homogeneous turbulence. *AIAA J.* **35**, 1030–1040.

https://doi.org/10.1017/S002211200500580X Published online by Cambridge University Press

Sarpkaya, T. & Daly, J. J. 1987 Effect of ambient turbulence on trailing vortices. *J. Aircraft* **24**, 399–404.

Sun, M. & Marshall, J. S. 2000 A flow visualization study of vortex interaction with the wake of a sphere. *Trans. ASME: J. Fluids Engng* **122**, 560–568.

Tombach, I. 1973 Observations of atmospheric effects on vortex wake behavior. *J. Aircraft* **10**, 641–646.

Vincent, A. & Meneguzzi, M. 1991 The spatial structure and statistical properties of homogeneous turbulence. *J. Fluid Mech.* **225**, 1–20.

https://doi.org/10.1017/S002211200500580X Published online by Cambridge University Press